Galileo's First Images of Jupiter and the Galilean Satellites

M. J. S. Belton,* J. W. Head III, A. P. Ingersoll, R. Greeley, A. S. McEwen, K. P. Klaasen, D. Senske, R. Pappalardo, G. Collins, A. R. Vasavada, R. Sullivan, D. Simonelli, P. Geissler, M. H. Carr, M. E. Davies, J. Veverka, P. J. Gierasch, D. Banfield, M. Bell, C. R. Chapman, C. Anger, R. Greenberg, G. Neukum, C. B. Pilcher, R. F. Beebe, J. A. Burns, F. Fanale, W. Ip, T. V. Johnson, D. Morrison, J. Moore, G. S. Orton, P. Thomas, R. A. West

The first images of Jupiter, Io, Europa, and Ganymede from the Galileo spacecraft reveal new information about Jupiter's Great Red Spot (GRS) and the surfaces of the Galilean satellites. Features similar to clusters of thunderstorms were found in the GRS. Nearby wave structures suggest that the GRS may be a shallow atmospheric feature. Changes in surface color and plume distribution indicate differences in resurfacing processes near hot spots on Io. Patchy emissions were seen while Io was in eclipse by Jupiter. The outer margins of prominent linear markings (triple bands) on Europa are diffuse, suggesting that material has been vented from fractures. Numerous small circular craters indicate localized areas of relatively old surface. Pervasive brittle deformation of an ice layer appears to have formed grooves on Ganymede. Dark terrain unexpectedly shows distinctive albedo variations to the limit of resolution.

The Galileo mission is a multidisciplinary international effort to explore the jovian system. Its primary objectives are to explore the atmosphere of the giant planet, the large Galilean satellites, and the powerful and dynamic environment created by Jupiter's large, rapidly rotating magnetic field (*1*). To accomplish these objectives the Galileo spacecraft consists of an orbiter, with both remote sensing and space physics instrumentation, and an atmospheric entry probe. On 7 December 1995 Galileo completed its long journey to Jupiter and was successfully inserted into its initial orbit following receipt of data from the probe.

A primary objective of Galileo's orbital mission is to determine the nature of the processes that generate and sustain the major features that are seen in Jupiter's atmosphere, as well as the evolutionary processes that led to the geological state of the surfaces of the Galilean satellites that were first revealed in the 1979 reconnaissance by the Voyager mission. Galileo's imaging exploration has the advantage of 2 years in orbit for atmospheric studies and, for the investigation of volcanic activity on Io, considerably longer than the two brief periods of the Voyager flybys. In addition, Galileo's many close satellite encounters yield images with surface resolutions that are improved by factors of several hundred over those from Voyager, enabling more definitive photogeologic and stereographic diagnosis of the possible origins of surface features. Galileo's imaging capability is also extended beyond Voyager's into the near-infrared spectral region, which because of the molecular and mineralogical spectral features found there, increases the diagnostic power of the images for determining cloud structure and the composition and microscopic state of satellite surfaces.

Voyager's reconnaissance transformed our understanding of the physical nature of the Galilean satellites and gave new interest to understanding the organization, generation, and stability of dynamical features and wave phenomena on Jupiter. The stark transition from superactive, tidally driven, silicate and sulfur volcanism on Jupiter's colorful inner Galilean satellite, Io, to the icy, cratered and furrowed, and blackened primitive wastes of Callisto, Jupiter's most distant Galilean moon, was a dramatic discovery. The sparsely cratered, apparently recently formed and delicately fractured icy mantle that may overlie a subsurface ocean on the second moon, Europa, contrasted enigmatically with the convoluted global systems of grooves and islands of ancient terrain found on the third moon, Ganymede. The goals of Galileo's imaging experiment address all of these topics. Here we present our initial results on grooved and ancient furrowed terrains on Ganymede, volcanic processes on Io (location and properties of active plumes, surface color mapping), and vertical atmospheric structure in the vicinity of the Great Red Spot (GRS). We also report on images taken during a distant encounter with Europa (156,000 km) that provide visible and near-infrared coverage over large parts of its north polar areas that were poorly seen by Voyager.

Observational sequence. The first high-resolution images of Jupiter and its satellites were received from the Galileo Solid State Imaging (SSI) system (*2*) 7 months after the spacecraft was inserted into orbit about Jupiter (Fig. 1) (*3*). Of 129 images recorded, 127 were successfully returned (*4*). These images are the first phase of an exploration (*5*) that should yield nearly 3000 images of Jupiter's atmospheric dynamics as well as the geological and photometric characteristics of its satellites (*6*). High-resolution imaging of Ganymede, as the prime target of the initial imaging, was allocated most of tape recorder space and downlink telemetry available to the SSI (*7*). Targeting was based on the 1979 Voyager reconnaissance (*8*).

The camera flight software and spacecraft command software was reprogrammed before the encounter to provide essential new capabilities (*9*). These performed well; only in the new camera exposure routine and in the application of the existing BARC (Block Adaptive Rate Controlled) data compression hardware to high-resolution Ganymede images (*10*) was anomalous performance observed. One Ganymede image (at 11 m per pixel resolution) showed unexplained smear; the absolute camera pointing at known surface features, while good to <2 mrad due to the stability of this spacecraft, caused small displacement of some images from the targeted

M. J. S. Belton, National Optical Astronomy Observatories, 950 North Cherry Ave, Tucson, AZ 85719, USA.
J. W. Head III, R. Pappalardo, G. Collins, Department of Geological Science, Brown University, Providence, RI 02912, USA.
A. P. Ingersoll and A. R. Vasavada, Department of Geology and Planetary Sciences, California Institute of Technology, Pasadena, CA 91125, USA.
R. Greeley and R. Sullivan, Department of Geology, Arizona State University, Tempe, AZ 85287-1414, USA.
A. S. McEwen, P. Geissler, R. Greenberg, Lunar and Planetary Laboratory, University of Arizona, Tucson, AZ 87721, USA.
K. P. Klaasen, D. Senske, T. V. Johnson, G. S. Orton, R. A. West, Jet Propulsion Laboratory, California Institute of Technology, Pasadena, CA 91109, USA.
D. Simonelli, J. Veverka, P. J. Gierasch, D. Banfield, M. Bell, J. A. Burns, P. Thomas, Department of Astronomy, Cornell University, Ithaca, NY 14853, USA.
M. H. Carr, U.S. Geological Survey, Menlo Park, CA 94025, USA.
M. E. Davies, RAND, Santa Monica, CA 90406, USA.
C. R. Chapman, Southwest Research Institute, Boulder, CO 80302, USA.
C. Anger, ITTRES Ltd, Calgary, Alberta TIY 5Z6, Canada.
G. Neukum, Institute for Planetary Exploration, Deutsche Forschunganstalt für Luft und Raumfahrt, Berlin, Germany.
C. B. Pilcher, National Aeronautical and Space Administration, Washington, DC 20546, USA.
R. F. Beebe, Department of Astronomy, New Mexico State University, Las Cruces, NM 88003, USA.
F. Fanale, Institute for Geophysics, University of Hawaii, Honolulu, HI 96822, USA.
W. Ip, Max Planck Institute für Aeronomie, Lindau, Germany.
D. Morrison and J. Moore, NASA Ames Research Center, Moffett Field, CA 94035, USA.

*To whom correspondence should be addressed. E-mail: belton@noao.edu

area; unexpectedly high photometric contrast in Ganymede images at very high resolution (11 to 80 m per pixel) and high sun illumination produced some localized pixel saturation. Camera performance was degraded because of particle irradiation from Jupiter's magnetosphere but at rates that are about one-half those of model predictions. The camera detector shows no obvious degradation from its passage through the inner magnetosphere at orbit insertion; currently we see a small number (~150) of damage sites (noise spikes), but these often anneal and disappear while other new damage sites are created.

Jupiter. The SSI system for imaging Jupiter's atmosphere provides both high spatial resolution and wide spectral coverage. At 30 km per pixel, the SSI can image cloud features whose horizontal scale is comparable to the atmospheric scale height. On Earth, such features are associated with deep moist convection (thunderstorms) and atmospheric waves. The SSI carries near-infrared filters centered at 732 and 886 nm (*2*), where methane gas is a moderate and strong absorber, respectively. Because Jupiter contains methane, scatterers (cloud particles) that lie deeper than a few bars are invisible at 732 nm, and scatterers that lie deeper than a few hundred millibars are invisible at 886 nm (*11*). Filters at 415 and 757 nm (between the methane absorption bands) complete the four-filter set used for most jovian imaging (*12*).

The sequences were designed to reveal the motions of the clouds down to the limit of resolution (*13*). During the encounter the GRS was imaged four times over an 11.5-hour period: Sequence 1 (S1) is near the center of the illuminated disk; S2 is near the terminator about 9 hours later; S3 is near the center of the illuminated disk 10.1 hours (slightly more than a full jovian rotation) after S1; and S4 is near the bright limb (edge) of the planet 11.5 hours after S1. Each sequence covers the GRS, usually with a 3 by 2 mosaic pattern. During the 70 minutes between S2 and S3 the 110 m/s winds around the GRS carry the cloud features a distance of 462 km—about 15 pixels. With precise knowledge of camera pointing, such displacements can be used to measure winds. The changing perspective as

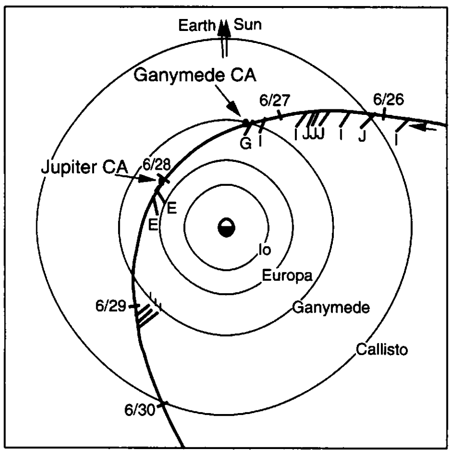

Fig. 1. Orbital trajectory showing the location of SSI observations for the G1 orbit. The lines along the spacecraft orbit show the position and direction from which each target was observed (G, Ganymede; E, Europa; I, Io; and J, Jupiter). Four very high resolution (up to 11 m per pixel) observations of Ganymede, not reported here, were made at the time of closest approach.

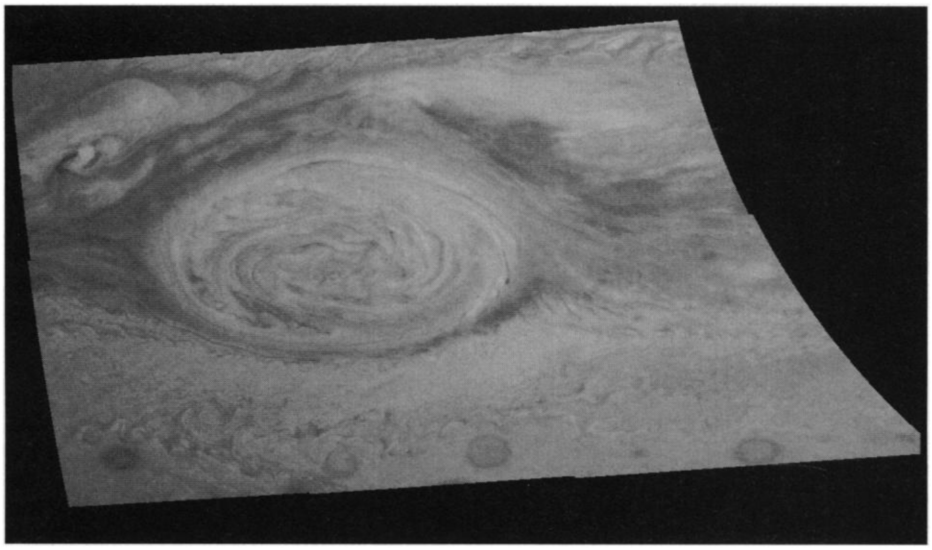

Fig. 2. Mosaic of Jupiter's GRS at 757 nm (near-infrared continuum). The six images of the mosaic are part of the S1 sequence (see text) that began at 4:18 UT on 26 June 1996. North is at the top. The map projection assigns equal distance to equal increments of longitude and planetocentric latitude. The long axis of the GRS is 20,000 km, and the counterclockwise winds around its periphery reach 110 m/s. Other features of interest are three smaller vortices to the south, a very bright cloud feature to the northwest, and the dark collar surrounding the GRS. From earlier Voyager, HST, and ground-based observations, the smaller ovals are known to be long-lived anticyclonic storms (vortices) like the GRS whose lifetimes are limited mainly by merging with other ovals (*13*).

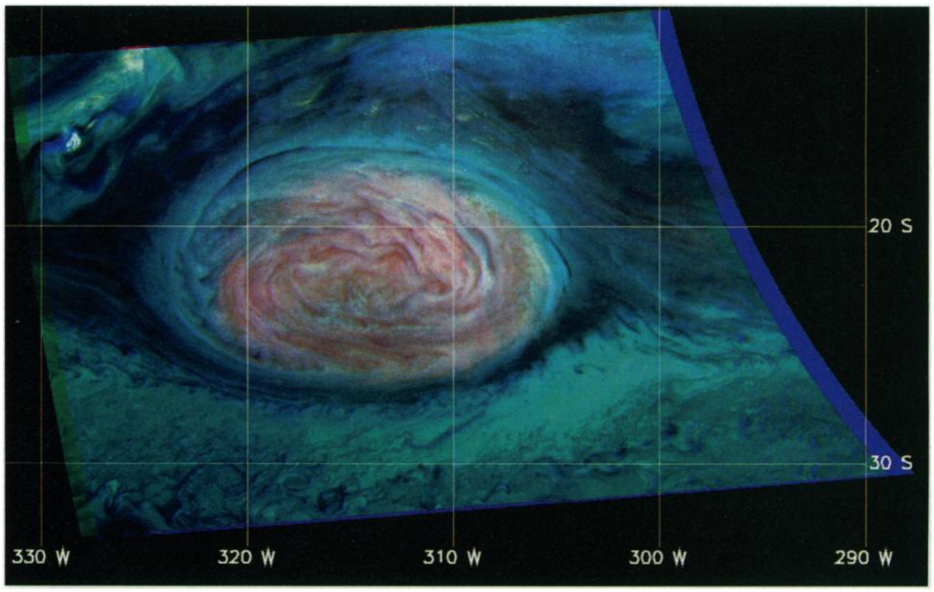

Fig. 3. False-color mosaic of Jupiter's GRS processed to reveal cloud-top heights. The six images of the mosaic are part of the S2 sequence (see text) that began at 13:18 universal time (UT) on 26 June 1996. Images taken through Galileo's near-infrared filters record sunlight beyond the visible range that penetrates to different depths in Jupiter's atmosphere before being reflected by clouds. Light at 757 nm, shown in blue, penetrates the deepest. Light at 732 nm, shown in green, penetrates to intermediate depths, and light at 886 nm, shown in red, penetrates to shallower depths before being absorbed by atmospheric methane. Therefore, blue areas are deep clouds; pink areas are high, thin hazes; and white areas are high, thick clouds.

the GRS crosses the illuminated disk during S2, S3, and S4 provides added information about cloud heights.

The S1 mosaic (Fig. 2) shows the primary cloud features in the GRS at this epoch. A false-color mosaic (Fig. 3) from the S2 sequence illustrates vertical properties of clouds in the vicinity of the GRS in the near-infrared. The pink area at the center of the GRS is a region of high, thin clouds—the small amount of scattering has a greater relative effect at 886 nm than at other wavelengths because the planet is normally dark at 886 nm as a result of the absorption of methane. The bright spot northwest of the GRS is a region of high, thick clouds—all of the light is scattered before it reaches deeper levels. The dark blue areas near the bright white spot are regions of low clouds—all the light at 732 and 886 nm penetrates deep to where it is absorbed. Finally, the dark brown area around the GRS is a thin haze over an otherwise low-cloud region.

Selected areas in the vicinity of the GRS that show details of individual cloud structures at high spatial resolution are shown in Fig. 4. Each of the six squares covers 4.8° of latitude (about 6000 km) and 4.8° of longitude. Photometric analysis of the bright white spot to the northwest of the GRS (Fig. 4D) suggests that it rises to at least 30 km above its surroundings. Voyager sequences (*14*) show similar spots forming west of the GRS and growing rapidly to diameters of 2000 km within 1 day. Usually they were sheared apart by opposing currents, a westward flow (70 m/s) at 15.4°S planetocentric latitude and an eastward flow (150 m/s) at 5.7°S. The Galileo near-infrared images, which provide more vertical discrimination, confirm the impression that they are convective features analogous to clusters of terrestrial thunderstorms (*15*). Although similar features were seen in Voyager images, the height of the features was not measured because the Voyager cameras did not have near-infrared filters.

Comparison of images from S2 and S3 of the area to the northeast of the GRS (314°W, 13°S), taken only 70 min apart, shows that many of the features changed (Fig. 4, A and B). Both the small size of the features and their rapid changes are reminiscent of terrestrial thunderstorms. However, their linear structure and 300-km spacing of the features are similar to slantwise convection on Earth, in which convective rolls are aligned in the direction of the wind (*16*). Slantwise convection, also known as symmetric baroclinic instability, occurs when the horizontal wind speed varies with altitude and the vertical temperature gradient is close to adiabatic. Some features are visible only at 732 nm (mid-level clouds), others visible only at 886 nm (high thin clouds, Fig. 4C), and still others are visible in both filters (high thick clouds).

A packet of mesoscale waves (wavelength of 300 km) is visible near 307°W, 15°S in the S1 image at 415 nm but seems to have disappeared 9 hours later at the time of S2 (Fig. 4, E and F). The wave packet is aligned approximately east-west, and the wave crests run north-south, even though the wind is from the southeast. If the waves result from a shear instability, the crests should be perpendicular to the wind shear, thus the wind below the cloud tops may be in a different direction from that at cloud tops. Any configuration in which the northward component is the same at the two levels but the east-west component is different will produce a wind shear that is in the east-west direction. A speculative interpretation is that the wind speed increases with depth and the wind direction becomes more nearly zonal (westward). If this is the case, then the GRS vortex is a relatively shallow structure.

Io. The SSI camera returned three sets of four-color full-disk images of Io at moderate phase angles (25° to 55°), two sets of three-color high-phase (~122°) crescent images, and two clear-filter (380 to 1050 nm) eclipse images with Io in Jupiter's shadow (Figs. 5 and 6). With spatial resolutions of 9 to 23 km per pixel, the images provide our best looks at Io since the Voyager flybys 17 years ago (*8*). The full-disk images, intended for color mapping of the surface and comparison with Voyager images, cover about 75% of Io's surface; coverage of the remaining area was acquired during the second encounter, which occurred on 6 September 1996. The high-phase images were intended primarily for color imaging of active volcanic plumes on the bright limb. The eclipse images (acquired with exposure times of 0.27 and 2.13 s) were designed to locate high-temperature hot spots and to image atmospheric and plume emissions.

Many surface changes have occurred since the Voyager era. The most dramatic come from new flows and pyroclastic deposits surrounding the shield volcano Ra Patera (*17*), near the Voyager-era volcanic plume named Marduk, from new pyroclastics near Euboea Fluctus, and from about 10 smaller (~100-km

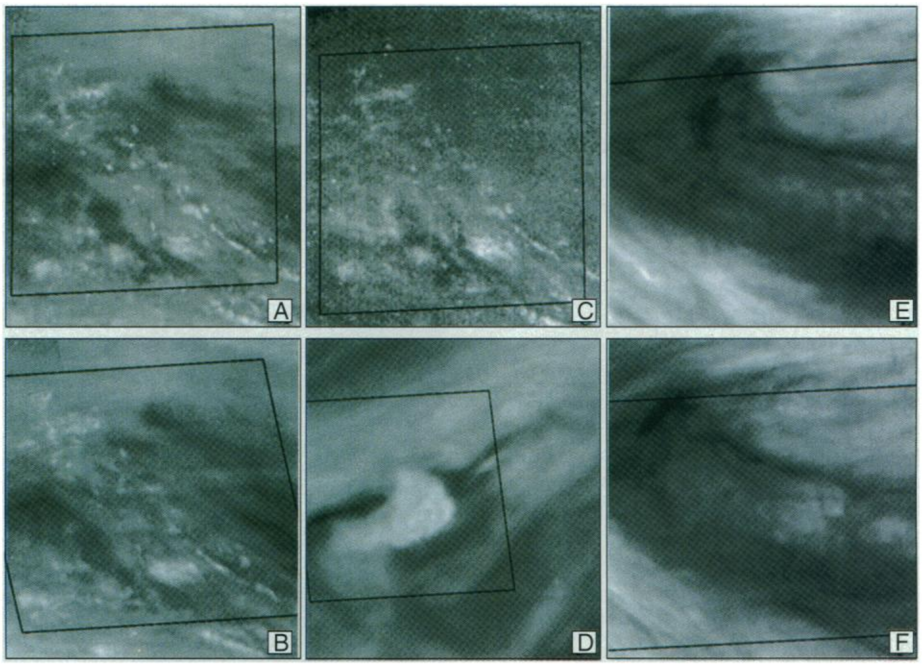

Fig. 4 (**A** and **B**). Time sequence of a convectively active region. These 732 nm (weak methane band) images cover an area 6000 km on a side centered at 13°S planetocentric latitude and 314°W longitude and were taken 70 minutes apart as part of the S2 (A) and S3 (B) sequences. The areas within the dark lines are "truth windows," which were transmitted to Earth with less data compression. Cloud features advect in the local wind field, which is parallel to the cloud streaks and toward the upper left corner. (**C**) Area at 314°W, 13°S in the strong methane band (886 nm) at the same time as the moderate methane band image (732 nm) at top left. Brightness differences are caused by the different depths of features in the two images. (**D**) The white spot to the northwest of the GRS in the 757-nm filter. Its appearance at different wavelengths suggests that the brightest elements are 30 km higher than the surrounding clouds. (**E** and **F**) Time sequence of a mesoscale wave. These violet (415 nm) images taken nine hours apart as part of the S1 (E) and S2 (F) sequences show the time evolution of an atmospheric wave northeast of the GRS at 15°S, 307°W. At least 15 crests with a spacing of 300 km are visible in the upper image, but they are much less apparent 9 hours later. The misalignment of the north-south wave crests with the observed northwest local wind may indicate a shift in wind direction with height.

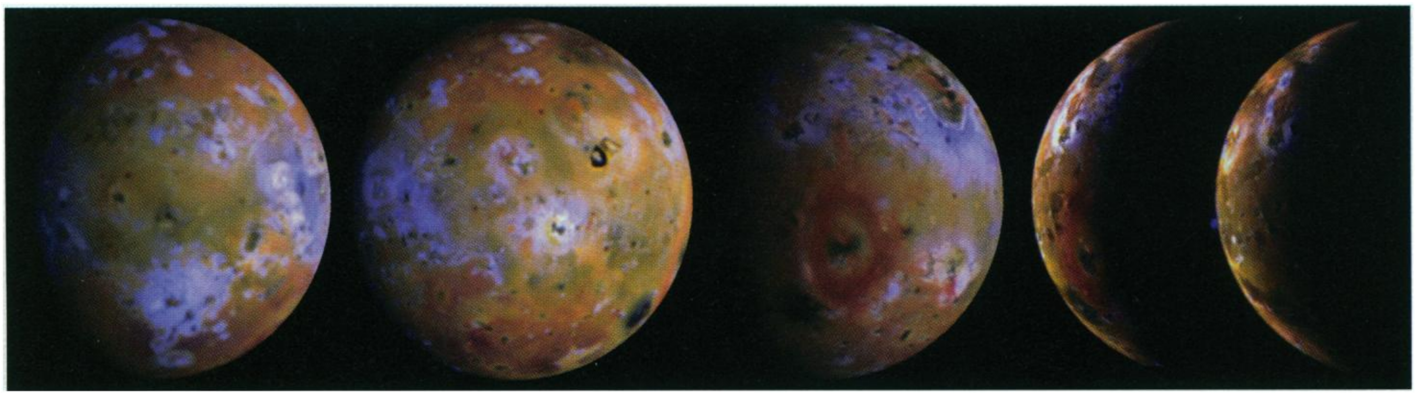

Fig. 5. Five color views of Io, in chronological order from left to right. Subspacecraft longitudes on Io (from left to right) are 69°, 338°, 264°, 211°, and 221° W. Color composed of red, green, and violet (for Io the central wavelengths are 664, 560, 418, respectively) bandpasses, but with the brightness of the violet bandpass increased to provide better color discrimination. Where images overlap, several features can be seen to change in relative brightness, perhaps due to unusual photometric scattering behavior or active phenomena.

scale) changes. The brightening at Ra Patera was earlier seen from Hubble Space Telescope (HST) images, and is known to have occurred between March 1994 and July 1995 (*18*). The presence of new bright yellow deposits with flowlike morphologies at Ra Patera and Marduk (Fig. 5) and the absence of intense hot spots at these locations (*19*) are consistent with sulfur flows, as has been previously proposed (*20*) for Ra Patera. In contrast, surface changes are much more subtle near the persistent high-temperature hot spots Loki and Kanehikili, which may be dominated by silicate volcanism (*21*). The differences in resurfacing and thermal emission indicate that a diversity of effusive eruptions occur on Io, perhaps including both sulfur and silicate magmas.

Several large-scale surface changes occurred between Voyagers 1 and 2, including deposition of Pele-sized plume features surrounding Surt and Aten Pateras and darkening of their caldera floors (*22*). In Galileo images these regions now appear more similar to those of Voyager 1. Such reversals of color changes over time scales of years to decades must be a result of phase transformations or sublimation of plume fallout and dark caldera floor materials.

The SSI color filters, when utilized for Io, have central wavelengths of 418 (violet), 560 (green), 664 (red), and 757 nm (near-infrared). Because Voyager coverage was restricted to wavelengths shorter than 600 nm, the longer wavelength Galileo data provide new information on Io's surface composition. Four distinctive spectral types appear to correspond to relatively recent deposits on Io: (i) dark materials in flows or on caldera floors, (ii) bright yellow flows, (iii) bright white patches (probably SO_2 frost), and (iv) intense reddish deposits.

HST observations showed that plume fallout deposits from Pele (*18*) had an intense red color and that polar regions were generally reddish (*23*). These features are also seen in the Galileo images. In that some fading of the plume deposits from Surt and Aten Patera would be likely over 17 years since Voyager, the intense reddish color of Pele's plume deposits suggests that the plume has been active recently. The reflectance spectra of these deposits may be best explained as due to small quantities of metastable short-chain elemental sulfur (S_3 or S_4) (*24*).

In addition to Pele's deposits, diffuse red materials (probably pyroclastics) are also seen near many other locations of active or recently active volcanism, such as Euboea Fluctus, Marduk, Aten Patera, and hot spots in Northwest Colchis Regio. Furthermore, red materials in the polar regions are seen to be patchy rather than uniform and appear to be due to volcanic pyroclastics rather than atmospheric condensation that would form true polar caps. We propose that pyroclastic eruptions are randomly placed and the red pyroclastics transform or sublimate more slowly in the colder polar regions.

Active plumes and hot spots. About half of the Voyager-era plumes appear to have been active during the initial encounter. Only two can be positively identified from observations against space on the bright limbs: a 100-km high plume at Ra Patera (not active during Voyager) and a plume near the location of Volund. The two Loki plumes are clearly not active, as there is no hint of material in high-

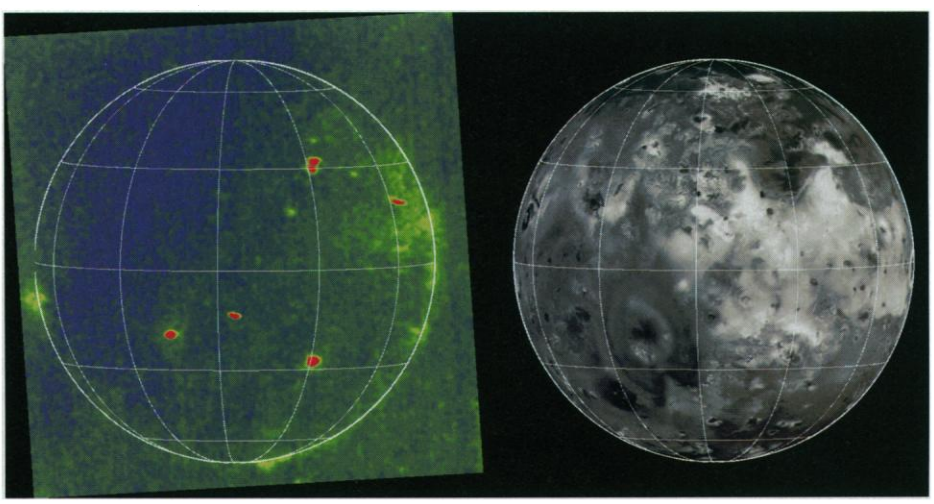

Fig. 6. A clear filter (380 to 1050 nm) 2.13-s exposure of Io taken in eclipse (**left**); brightnesses are color coded (red is highest intensity, blue is zero intensity). A Voyager image mosaic (**right**) is shown with an identical scale and projection. North is to the top. In the Galileo image (left) small red ovals and perhaps some small green areas are likely due to thermal emission near 1000 nm from volcanic hot spots, whereas diffuse greenish areas seen near the limb are probably auroral or airglow emissions of neutrals or ions in volcanic plumes (*28*) and Io's patchy atmosphere (*30*). The grid marks are at 30° intervals of latitude and longitude; central longitude is 235°. As a result of the relatively long exposure, the image has been smeared by about 3 pixels by 8 pixels. This image was taken from a range of 1,035,000 km; unsmeared, it would have a resolution of 10.5 km per pixel.

phase images targeted specifically for these plumes. We also acquired Pele on the bright limb, but the only evidence for a plume is a small enhancement in the green filter with about the right location, shape, and size. There is no sign of Pele's plume in the other three filters or in the eclipse image. If Pele is a purely gaseous stealth plume (*25*), then its characteristics differ from those predicted. We interpret the dark jets seen against Io's disk to indicate that the Marduk plume is active. The Amirani plume shows no enhancement just beyond the terminator and may be inactive. We have no reliable information on the activity of Prometheus, Maui, or Masubi so far.

The eclipse images reveal at least five hot spots: Pele, Marduk, and three hot spots in NW Colchis Regio (Fig. 6). The Pele hot spot is more than 20 times as intense than the others, perhaps because it is a site of active siliceous volcanism. All of the hot spots fall precisely on low-albedo surface units, confirming this suspected relationship (*26*). Pele was the hottest feature observed by Voyager, with a minimum temperature of 600 K (*27*). From the eclipse image we have determined minimum temperatures of 700 K for Pele and 600 K for the other spots.

Atmospheric emissions. In addition to discrete hot spots, the eclipse image also reveals presumed auroral glows near Ra Patera's plume (directly on the limb), an extended glow around the Volund plume (covering a much larger area than the visible plume), and a thin layer outlining the limb on Io's leading hemisphere and south polar region. The emission layer at the limb is evidently not related to a direct impingement of magnetospheric particles because impingement occurs on the trailing hemisphere as a result of Jupiter's rapid rotation. Similar emissions near plumes were seen in a Voyager eclipse image (*28*), but through a narrower spectral bandpass (380 to 600 nm). The thickness of the limb glow is generally comparable to the image smear, indicating that the emitting layer is very thin, less than about 20 km. There is no obvious indication in the eclipse image that the layer is optically thick. Furthermore, the layer is located near, and possibly extends to, the surface (Fig. 6). The Prometheus plume, if active, could contribute to the glow near the eastern limb. Ra Patera was also found to glow in the red bandpass [full width at half maximum (664 ± 30 nm) FWHM], seen beyond the terminator in a full-disk image, possibly indicating a contribution from forbidden [OI] emission near 630 nm (*29*). No evidence for stealth plumes (*25*) is apparent. No atmospheric emissions are, for example, seen in the vicinity of Pele, which has no obvious plume and for which strong effusion of SO_2 would be consistent with Earth-based millimeter-wave and ultraviolet (UV) observations (*30*).

Europa. Europa was photographed during the two Voyager flybys, but resolution and coverage were poor (*8*, *31*). Galileo returned 12 images of the northern hemisphere between longitudes 160° and 290°W, providing high-resolution data (compare Figs. 7 through 9) and color information in six bands (effective wavelengths of 416, 559, 664, 757, 888, and 989 nm) over a wide area.

Light and dark bands, generally considered to represent zones of tectonic deformation, constitute the principal structural features seen (Figs. 7 and 8). Triple bands, linear regions of lower albedo that are typically 10 to 20 km wide with a medial high albedo stripe, are evident. The medial stripes of triple bands are typically 5% brighter than the flanking dark materials in the youngest triple bands. Age relations (shown by crosscutting relations) suggest that the dark zones of triple bands brighten with time and approach, or surpass, the albedo of the background plains in which they occur. The SSI images show that the outer margins of triple bands are diffuse over distances of 10 km. Consequently, formation models (*34*, *37*) involving primarily tectonic processes forming sharp outer boundaries seem less plausible. High-velocity venting of material from fractures could produce the diffuse outer margins if clastic materials concentrate close to the vent and thin outward to feather edges. Initial eruptions could involve gases (*38*), and perhaps liquids (contaminated with rocky material), derived from the icy crust. As this material emerges, the volatiles are lost to space and the rocky debris showers onto the surface.

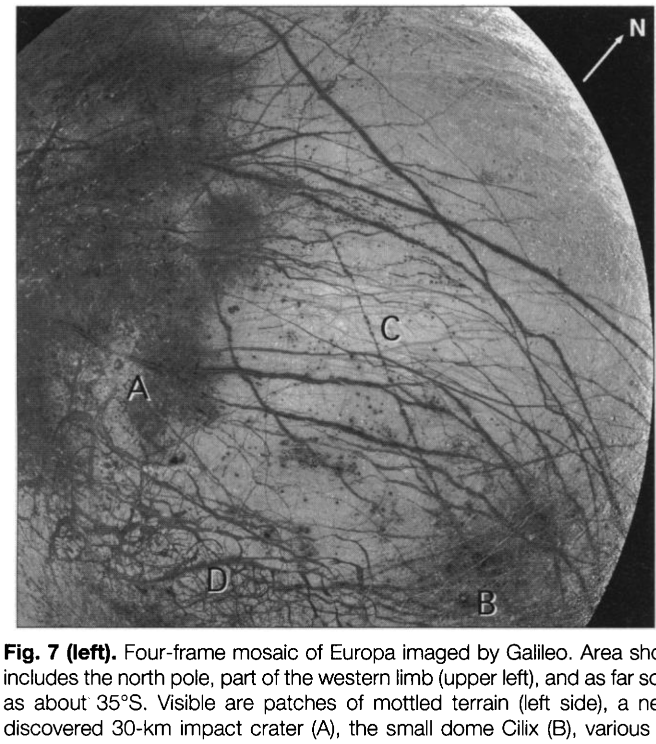

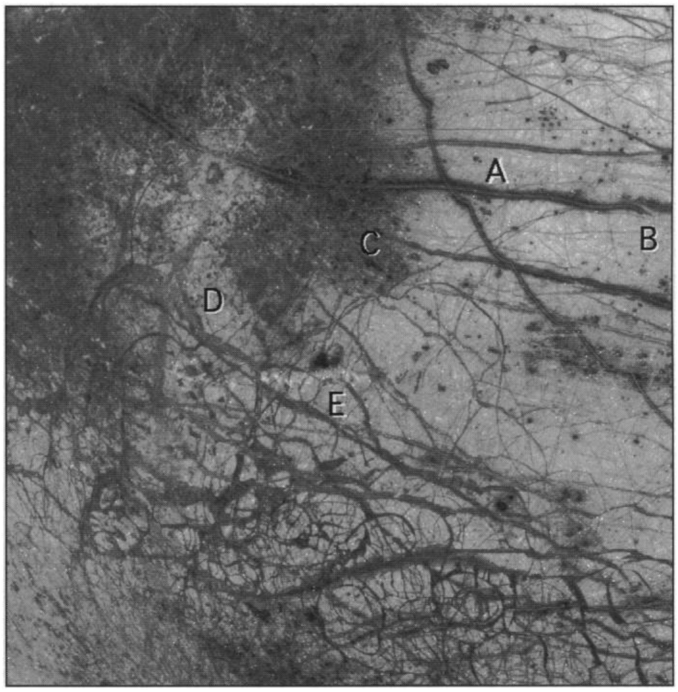

Fig. 7 (left). Four-frame mosaic of Europa imaged by Galileo. Area shown includes the north pole, part of the western limb (upper left), and as far south as about 35°S. Visible are patches of mottled terrain (left side), a newly discovered 30-km impact crater (A), the small dome Cilix (B), various crisscrossing lineaments (some composed of aligned dark spots) (C), and highly disrupted terrain (D) in the antijovian region. **Fig. 8 (right).** View of Europa showing part of the equatorial region. Visible are triple bands with diffuse outer margins (A), a triple band that appears to be offset (B), and mottled terrain (C). Also visible are gray bands (D) and aligned high-albedo patches (E) that appear to radiate from a common source visible on low-resolution Voyager images at 271°W, 26°S, inferred to be an impact crater.

With continued eruption, the conduit may be cleared of contaminants, and cleaner slush or ductile ice may be exposed to the surface where it freezes, forming the bright medial band. Rhadamanthys Linea (Fig. 7), a 2000-km-long dark band marked by dark patches ranging from a few kilometers to ~30 km, may be an expression of this process.

Other structural features observed (Figs. 7 and 8) include bright bands, narrow ridges, moderate-albedo bands, and highly fractured regions. Bright bands crosscut nearly all other features and are therefore among the youngest structures on the surface. Close to the terminator where relief can be seen, many bright bands form narrow ridges. Moderate-albedo bands are reminiscent of bright grooved-and-ridged terrain on Ganymede and could represent disruption of ice crust and replacement by relatively fresher ice or slush. Terrain in the area observed by the Galileo spacecraft immediately south of the equator and to the west of the anti-jovian region is highly fractured and disrupted by dark linear and curvilinear features and dark wedges within the higher albedo crust. Similar features seen less sharply by Voyager in an adjoining area to the east were proposed to represent pull-apart zones (*39*) in which the crust was extended and repositioned, reminiscent of floes and leads within terrestrial polar ice packs. The most prominent dark fractures are spaced at intervals of 75 to 150 km. These features suggest a possible origin due to relatively small-scale subcrustal convection at the time of disruption.

Other features include small knobs, raised platformlike areas as large as 35 km across, and low-albedo spots (freckles), many of which have bright central cores. Freckles could have an origin similar to that proposed above for triple bands (local eruptions or intrusions by dirty ice). The most prominent positive-relief feature is Cilix. Identified on Voyager images as a crater, Cilix is seen in the Galileo images to be a high-albedo knob some 16 km across surrounded by a moat of lower albedo material. The morphology of Cilex is similar to central domes on some impact craters on Ganymede (*40*) and Cilix might also have an impact origin. A stereoscopic combination of Galileo and Voyager images suggests a relief of about 1 km for Cilix and 2 km for an unnamed 13-km-diameter knob (33.5°N, 169.5°W).

Impact features. Less than a dozen possible impact features on Europa were identified from Voyager data. Galileo images show some additional features that may be of impact origin. The most prominent is a fresh 30-km crater centered at 240°W, 2°N, with ejecta superposed on the triple band Belus Linea. This impact appears to have penetrated through dark mottled terrain into bright, presumably ice-rich materials, forming discontinuous rays on the surrounding terrain for distances exceeding 100 km. Other discontinuous, but radially aligned, high-albedo patches are visible in the western and southwestern parts of the Galileo coverage (Fig. 7). These appear to radiate from a common source out of view to the southwest. Low-resolution Voyager data suggest that the source is a dark spot surrounded by a broad bright annulus centered at 271°W, 26°S, presumably a fresh impact crater (*41*).

Numerous shallow depressions with diameters of 10 km or less can be seen in some areas of the terminator zone. Some of these have irregular shapes. Many others are circular, and some have slightly raised rims, a characteristic of impact craters. If this interpretation is correct, these areas would be older than the age inferred from Voyager data. Other areas observed under comparable illumination and resolution are smooth and lack depressions, indicating local, more recent resurfacing.

Multispectral coverage at wavelengths between 416 and 989 nm reveals an unexpected division of Europa's bright icy plains into two units, which, although almost indistinguishable at visible wavelengths, are spectrally distinct in the near infrared (Fig. 9). The spectral reflectance of the contaminated ice component of Europa's crust, triple bands, brown spots, and other low-albedo features exhibit steep positive spectral slopes (red color) at visible wavelengths and are bright with relatively neutral color in the near-infrared (near 888 nm), where their reflectance is at a maximum. The bright plains (blue shades in Fig. 9) are seen to subdivide into two units that reverse contrast with increasing wavelength. The darker near-infrared regions have a relatively flat spectral reflectance at visible wavelengths and a pronounced absorption near 989 nm. The brighter near-infrared regions, not previously identified, are intermediate in color between the brown contaminants in the ice and the infrared-dark plains, and appear to be mixtures of the two (*42*). The higher infrared reflectivity in these regions may be the result of a reduction in grain size of the non-ice component, the icy matrix, or both.

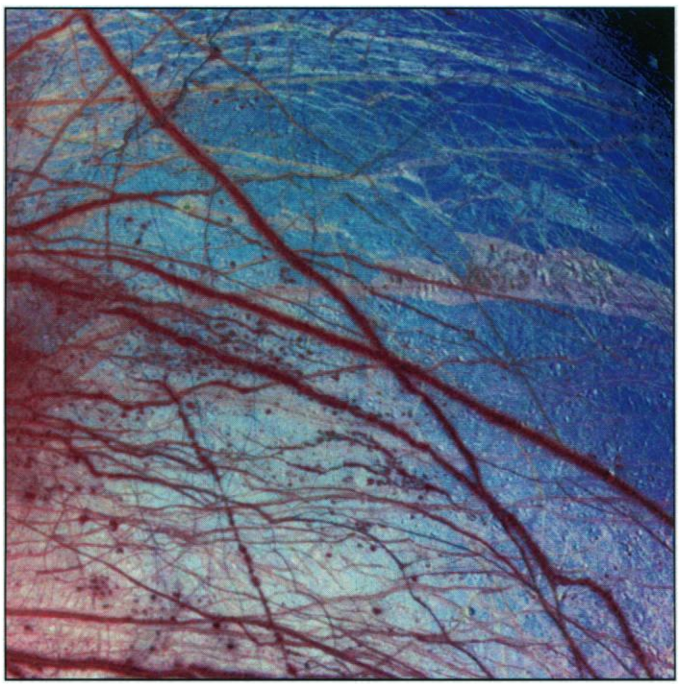

Fig. 9. False-color composite picture of the Minos Linea region of Europa, produced from images with effective wavelengths at 989, 757, and 559 nm. The spatial resolution in the individual images ranges from 1.6 to 3.3 km per pixel. The area covered, centered at 45°N, 221°W, is about 1260 km across. Triple bands, lineae, and mottled terrains appear in brown and reddish hues, indicating the presence of contaminants in the ice. The icy plains (bluish hues) subdivide into units with different albedos at infrared wavelengths probably because of differences in the grain size of the ice.

Ganymede. The SSI observations focused on the two main terrain types on this satellite. We report here on high-resolution (70 to 80 m per pixel) characterization of samples of both bright (Uruk Sulcus) and dark (Galileo Regio) terrain (Figs. 10 and 11).

As seen by Voyager, the bright terrain consists of smooth plains and linear grooves (troughs) averaging about 4 km in width arranged in a global network (*43*). The dramatic improvement in the resolution of Galileo images is illustrated in Fig. 12. The several bright grooves visible in the Voyager image, spaced a few kilometers apart, can be seen in the Galileo images to be composed of several tens of ridges and troughs with an average spacing of a few hundred meters. The individual ridges are long and relatively continuous and they appear generally triangular in cross section. This landform is evidence that pervasive brittle deformation of an ice layer has occurred during the formation of grooves in this part of Uruk Sulcus. There is no evidence that these features formed by viscous relaxation, large-scale mass wasting, constructional ice volca-

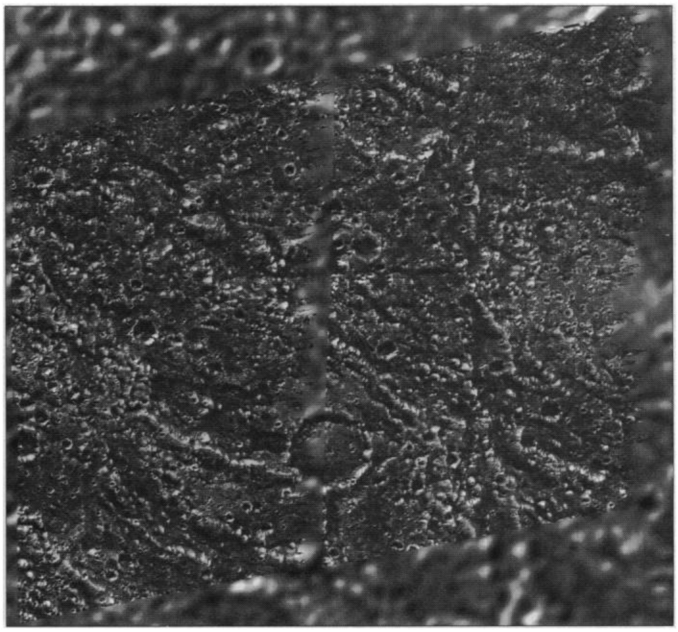

Fig. 10 (left). Four-frame mosaic of the Uruk Sulcus region (11.1°N, 168.9°W) on Ganymede at ~74 m per pixel and taken through the clear filter. The gap running roughly north-south between the two parts of the mosaic is due to excessive line truncation by the SSI camera hardware data compressor (*10*). **Fig. 11 (right).** Four-frame mosaic of the Galileo Regio region (18.4°N, 149.0°W) on Ganymede at ~80 m per pixel and taken through the clear filter. The gap running roughly north-south between the two parts of the mosaic is due to excessive line truncation by the SSI camera hardware data compressor (*10*).

nism, or surface deformation attributed to ice plutonism (*44*). The shapes of the structures are not typical of simple horst and graben structure. The considerably smaller spacing of the ridges and troughs in this groove lane compared to that interpreted from Voyager means that the deformed layer is likely to be thinner than previously thought (*45*).

On the right-hand portion of the Galileo image is a polygon of grooved terrain with internal structures generally trending north-south. This area appears to be relatively smoother at both Voyager and Galileo resolution than the throughgoing groove lane and is similar to the terrain thought to have represented relatively recent cryovolcanic resurfacing of grooved polygons (*46*, *47*). We find no evidence for geologically recent resurfacing. The smoother region has a higher density of impact craters, indicating an older age than that of the adjacent groove lane, and the southern margin is cut by ridges and troughs of the groove lane. Parallel fractures in the polygon become troughs and ridges over a lateral distance of several kilometers.

Differences between the structures of the groove lane and the adjacent polygon suggest that the tectonic style has changed with time. In the polygon region, ridges and grooves are broad and widely spaced and appear less distinctive; they are reminiscent of blocks typical of horst and graben formation, but the high crater density obscures important details. Viscous relaxation may be important, but the absence of any evidence for broad distortion of crater shape suggests that the difference is due to a change in style rather than relaxation. Although it has been suggested that the volcanic flooding of rift zones produced the broad lanes of bright terrain (*47*, *48*), we see no cryovolcanic activity (for example, smooth unmodified plains, lobate flow fronts, flooded and embayed terrain, or pyroclastic mantling). Instead, sequential and pervasive tectonic deformation dominates the surfaces of essentially all units in this part of Uruk Sulcus. These images also provide information on the sequence of events in bright terrain units and their general stratigraphy. The clear tectonic crosscutting relationships between the polygons and lanes (Fig. 12) are supported by crater density estimates in the two areas.

As seen in Voyager images, dark terrain consists of ancient, heavily cratered crust distributed across the satellite as a series of

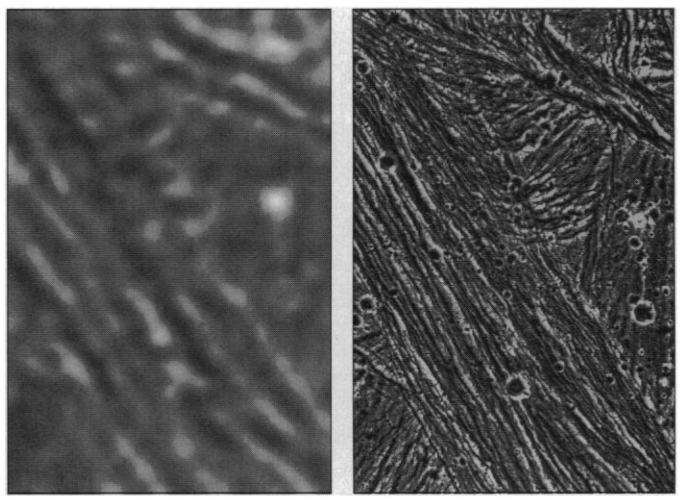

Fig. 12. Comparison of a 35 km by 55 km part of Uruk Sulcus (~10°N, 167° W) at Voyager (**left**) and Galileo (**right**) resolution. The Voyager 2 frame is at a resolution of ~1.1 km per pixel. The Galileo image taken during first Ganymede flyby has a resolution of ~74 m per pixel, more than 16 times that of the Voyager image. In the Voyager frame, linelike bright and dark bands can be seen, but their detailed structure and origin are not clear. In the Galileo image, each band is now seen to be composed of many smaller ridges. In each of these frames, north is to the top, and the sun illuminates the surface from the lower left nearly overhead (about 77° above the horizon).

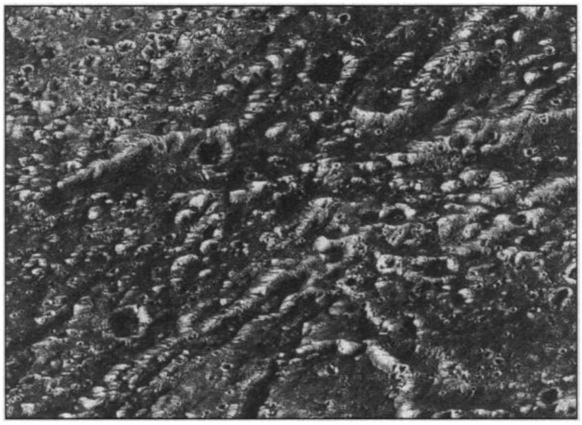

Fig. 13. Dark terrain in Galileo Regio (~18°N, 147°W) through the clear filter. At the lower margin, half of a 19-km-diameter crater is visible. The dark and bright lines running from lower left to upper right and from left to right are furrows. In this view, north is to the left, and the sun illuminates the surface from the lower right about 58° above the horizon. Area shown is about 46 km by 64 km. Resolution is ~80 m per pixel.

rounded, polygonal, and irregular fragments of various sizes, all surrounded by deposits of younger, bright grooved terrain (*49*). Dark terrain is locally cut by a series of linear, rimmed furrows hundreds of kilometers long that comprise several systems with various orientations and curvature (*50*). The abundant impact craters in dark terrain vary in morphology and states of degradation. The area imaged in Galileo Regio, the largest dark terrain on Ganymede, is characterized (Fig. 13) by variations in its albedo (*46, 51*), impact craters of various sizes and states of degradation, and two different intersecting furrow sets. The walls of most of the craters, from only a few hundred meters in diameter up to the prominent impact crater in Fig. 13, are brighter than their surroundings; the streaking of dark lines down the walls and the apparent accumulation of dark material on lower slopes and floors indicates that these are not just photometric effects, but instead represent topography. The raised rims and interior walls of furrows are also brighter than surrounding dark terrain; pitted, cratered, and streaked rims and walls appear to have shed dark material into adjacent surrounding lows. Isolated knobs, some apparently the rim crests of highly degraded craters, are also bright and may have also shed dark material from their upper slopes. Finally, a different style of heterogeneity is seen in the intervening plains; dark plains are located in the flattest areas among these other features, and bright plains form a contiguous deposit several tens of kilometers across, as shown in the upper left of Fig. 13.

The albedo of the dark terrain varies on a scale of hundreds of meters to kilometers. These observations could be interpreted to mean that the source of the dark albedo is the addition of some material from above, which is then shed off the steep slopes to accumulate in lows. However, the albedo of dark terrain varies with latitude and distance from the leading hemisphere of the satellite (*52*). Further analysis must await acquisition of images of dark terrain targets on other parts of Ganymede during later encounters. There is a wide range of degradation states of craters in Fig. 13. Some have more superposed craters and others appear shallower, perhaps because of viscous relaxation of the ice or infilling. A striking feature of many of the craters is that their interior walls are marked by generally north-south trending, parallel bright and dark streaks, perhaps because a preexisting fracture pattern has been accentuated by downslope movement of material. These features do not cut adjacent bright and dark plains units. If confirmed by subsequent observations, the presence of this set of fractures would suggest that regional tectonic deformation occurred in the dark terrain early in its history. Such tectonic activity could be part of an explanation for the lower crater density in the dark terrain on Ganymede relative to that on Callisto.

Furrow walls are heavily cratered (Fig. 13), dark material is shed off highs into lows, and the floors of furrows are filled with dark plains. Furrow raised rims are prominent, and their continuity is disrupted both by preexisting crater topography and by impacts that postdate furrow formation. Despite their degradation state, the north-south trending furrow can be seen to crosscut the northwest-southeast trending set, confirming interpretations from Voyager data (*52, 53*).

REFERENCES AND NOTES

1. T. V. Johnson *et al.*, *Space Sci. Rev.*, **60**, 3 (1993).
2. M. J. S. Belton *et al.*, *ibid.*, p. 413; K. P. Klaasen *et al.*, *Opt. Eng.* **23**, no. 3, 334 (1984). The effective wavelengths of the SSI filters are dependent on the spectrum of the target. We name the filters according to their effective wavelength for integrated sunlight: Clear (628 nm); violet (414 nm); green (559 nm); red (664 nm); 731, 757, and 888 nm; and 1 μm (990 nm). Where the effective wavelengths differ appreciably for a given target we have noted the appropriate wavelength in the text.
3. The Galileo spacecraft achieved orbit on 7 December 1995. Although images of Io, Europa, and Jupiter were scheduled to be taken near this time, most of these were not recorded because of a tape recorder malfunction on 11 October 1995, just following the acquisition of the first Jupiter approach images. These Jupiter images remain on the tape but in a region that cannot be safely accessed. Galileo's central computer was reprogrammed partly to provide an essential capability to compress SSI images before their transmission to Earth on the spacecraft's low-gain antenna.
4. According to the initial spacecraft operational flight rules, only one pass through the tape recorder was to be allowed following the Ganymede 1 encounter. This would have limited the number of returned images to about 117 and excluded most of the Europa coverage. However, because of technical problems with other experiments, four such passes were performed.
5. M. H. Carr *et al.*, *J. Geophys. Res.* **100**, 18935 (1995).
6. The Galileo nominal mission, which ends on 31 December 1997, after 10 orbits, should return about 1500 images. However, the option exists with the current predictions for propellant usage and lifetime against failure due to radiation damage to extend the mission by 2 years. The SSI has examined a concept (the Galileo Europa Mission) that would return an additional 1500 images, mainly of Europa but also including very high resolution images (~10 m per pixel) of Io not possible during the prime mission.
7. SSI was allotted 46 and 23% of the tape recorder space and downlink capability; of this, the Ganymede observations were allotted 47 and 51%, respectively.
8. The initial Voyager imaging is reported in B. A. Smith *et al.*, *Science* **204**, 951 (1979), and B. A. Smith *et al.*, *ibid.* **206**, 927 (1979).
9. The new capabilities that were used in the sequence are (i) a modified 2 by 2 pixel summation mode that includes pre-exposure light flood (primarily used for Jupiter atmospheric images), (ii) a half-frame readout mode (used primarily for Io monitoring) and (iii) an Integer Cosine Transform (ICT) data compression routine. ICT was applied to all atmospheric images and most satellite images; for the highest resolution images, the SSI hardware compressor [BARC, or "Block Allocation Rate Controlled," R. F. Rice *et al.*, *Proc. National Telemetering Conference*, Washington, DC, (1979)] was used in the rate-controlled mode.
10. The exposure fault was discovered from the Europa mosaics, which were found to be underexposed by about a factor of 2 relative to predictions. This problem is understood and is being corrected. The BARC compressor problem, which is still not completely understood, was made evident by the large photometric contrast at high spatial frequencies seen in the Uruk Sulcus and Galileo Regio images of Ganymede. The compressor works by first truncating up to three least significant bits (LSBs) per pixel in an image line and then, if the compression achieved is not sufficient, truncating the last pixels' readout in a line. The photometric activity in these pictures was such that the compressor was pushed into truncating lines. Examination of the LSBs showed that the compressor did not consistently first truncate them to the three bit level. As a result, these images suffer from shortened lines, from the normal 800 samples per line to about 540.
11. E. Karkoschka, *Icarus* **111**, 171 (1994).
12. For studies of jovian cloud structure, see D. Banfield *et al.*, *Icarus*, in press; F. M. Flasar *et al.*, *J. Geophys. Res.* **86**, 8759 (1981); R. A. West *et al.*, *Icarus* **65**, 161 (1990).
13. M.-M. MacLow and A. P. Ingersoll, *Icarus* **65**, 353 (1990); for a review of jovian atmospheric dynamics, see A. P. Ingersoll, *Science* **248**, 308 (1990).
14. R. Beebe *et al.*, in *Time-Variable Phenomena in the Jovian System*, M. J. S. Belton, R. A. West, J. Rahe, Eds. (*NASA SP-494*, National Aeronautics and Space Administration, Washington, DC, 1987), p. 245.
15. R. A. Houze Jr., *Cloud Dynamics* (Academic Press, San Diego, CA, 1993).
16. K. Emanuel, *Atmospheric Convection* (Oxford Univ. Press, New York, 1994).
17. R. Greeley *et al.*, *U.S. Geol. Surv. Map I-1949* (1988).
18. J. R. Spencer *et al.*, in preparation.
19. Based on ground-based observations taken at

NASA's Infrared Telescope Facility (IRTF) on 3 June 1996 by J. R. Spencer, personal communication.
20. D. C. Pieri *et al.*, *Icarus* **60**, 685 (1984).
21. D. L. Blaney *et al.*, *ibid.* **113**, 220 (1995); J. R. Spencer and N. M. Schneider, *Annu. Rev. Earth Planet. Sci.* **24**, 125 (1996).
22. A. S. McEwen and L. A. Soderblom, *Icarus* **55**, 191 (1983).
23. R. B. Minton, *Comm. Lunar Planet. Lab* **10**, 35 (1973).
24. R. M. Nelson and B. W. Hapke, *Icarus* **36**, 304 (1978).
25. T. V. Johnson *et al.*, *Geophys. Res. Lett.* **22**, 3293 (1995).
26. A. S. McEwen *et al.*, *J. Geophys. Res.* **90**, 12345 (1985).
27. J. C. Pearl and W. M. Sinton, in *Satellites of Jupiter*, D. Morrison, Ed. (Univ. of Arizona Press, Tucson, 1982), p. 724; D. Morrison and C. Telesco, *Icarus* **44**, 226 (1980).
28. A. F. Cook *et al.*, *Science* **211**, 1419 (1981); the Voyager wide-angle camera was sensitive to emissions between 380 and 600 nm. The SSI camera is sensitive to emissions in a much wider band, 380 to 1050 nm.
29. F. Scherb and W. H. Smyth, *J. Geophys. Res.* **98**, 18729 (1993).
30. E. Lellouch *et al.*, *Icarus* **98**, 271 (1992); G. Ballester *et al.*, *ibid.* **111**, 2 (1994); E. Lellouch, *ibid.*, in press; P. Sartoretti *et al.*, *ibid.*, in press.
31. B. K. Lucchitta and L. A. Soderblom, in *Satellites of Jupiter*, D. Morrison, Ed. (Univ. of Arizona Press, Tucson, 1982), p. 521; M. C. Malin and D. C. Pieri in *Satellites*, J. A. Burns and M. S. Matthews, Eds. (Univ. of Arizona Press, Tucson, 1990), p. 689. With a diameter of 3138 km and a mean density of 3040 kg/m^3, Europa is comparable in many respects to Earth's moon but contains at least 5% by mass of water (*32*). Earth-based spectroscopy shows the surface to be predominantly water ice (*33*). Although the water could be contained mostly in hydrated minerals (*34*), most models of the interior involve an outer shell of water as thick as 100 km, parts of which could be liquid (*35*). Local darkening of the surface could result from ice weathering and contamination by rocky materials (*36*). The general paucity of impact craters observed in the Voyager data suggested a youthful surface and the possibility of recent, or even active, resurfacing.
32. G. Schubert *et al.*, in *Satellites*, J. A. Burns and M. S. Matthews, Eds. (Univ. of Arizona Press, Tucson, 1990), p. 224.
33. C. B. Pilcher *et al.*, *Science* **178**, 1087 (1972).
34. A. A. Finnerty *et al.*, *Nature* **289**, 24 (1981).
35. P. Cassen *et al.*, *Geophys. Res. Lett.* **6**, 731(1979); G. W. Ojakangas and D. J. Stevenson, *Icarus* **81**, 220 (1989).
36. A. S. McEwen, *J. Geophys. Res.* **91**, 8077 (1990).
37. M. P. Golombek and E. Bruckenthal, *Lunar Planet. Sci.* **XIV**, 251 (1983).
38. G. D. Crawford and D. J. Stevenson, *Icarus* **73**, 66 (1988).
39. P. M. Schenk and W. B. McKinnon, *ibid.* **79**, 75 (1989).
40. P. H. Schenk, *J. Geophys. Res.* **98**, 7475 (1993).
41. A. S. McEwen, *Icarus* **81**, 220 (1990).
42. T. V. Johnson *et al.*, *J. Geophys. Res.* **88**, 5789 (1983); A. S. McEwen, *ibid.* **91**, 8077 (1986); D. Domingue and B. Hapke, *Icarus* **99**, 70 (1992).
43. B. Lucchitta, *Icarus* **44**, 481 (1980); E. Shoemaker *et al.*, in *The Satellites of Jupiter*, D. Morrison, Ed. (Univ. of Arizona Press, Tucson, 1982), p. 435.
44. Post-Voyager discussion of graben, modified tension fractures, and ductile necking features can be found in the following: J. Fink and R. Fletcher, *NASA Tech. Memo. TM-84211* (1981), p. 51; E. Shoemaker *et al.*, in *The Satellites of Jupiter*, D. Morrison, Ed. (Univ. of Arizona Press, Tucson, 1982), p. 435; E. M. Parmentier *et al.*, *Nature* **395**, 290 (1982); and S. W. Squyres, *Icarus* **52**, 545 (1982). Mass wasting and differences in strain rate or thickness of the lithosphere are discussed by Parmentier *et al.* and Squyres. Constructional ice-volcanism or surface deformation due to ice plutonism in underlying fractures is discussed by S. Croft *et al.*, *Icarus* **73**, 279 (1988).
45. See, for example, the discussion by S. W. Squyres and S. K. Croft in *Satellites*, J. A. Burns and M. S. Matthews, Eds. (Univ. of Arizona Press, Tucson, 1990), p. 293.
46. M. P. Golombek and M. Allison, *Geophys. Res. Lett.* **8**, 1139 (1981); S. J. Murchie *et al.*, *J. Geophys. Res.* **91**, E222 (1990); E. M. Parmentier *et al.*, *Nature* **295**, 290 (1982).
47. J. E. Guest *et al.*, *U.S. Geol. Surv. Misc. Invest. Ser. Map I-1934* (1988).
48. S. J. Murchie *et al.*, *J. Geophys. Res.* **91**, E222 (1990); R. Cassachia and R. Strom, *ibid.* **89**, B419 (1984); P. Shenk and W. McKinnon, *Icarus* **72**, 209 (1987); M. Zube and E. Parmentier, *ibid.* **60**, 200 (1984); E. M. Shumaker *et al.*, in *Satellites of Jupiter*, D. Morrison, Ed. (Univ. of Arizona Press, Tucson, 1932), p. 435.
49. E. M. Shoemaker *et al.*, in *Satellites of Jupiter*, D. Morrison, Ed. (Univ. of Arizona Press, Tucson, 1982), p. 435.
50. S. J. Murchie *et al.*, *J. Geophys. Res.*, **91**, E222 (1990).
51. B. Lucchitta *et al.*, *U.S. Geol. Surv. Misc. Inv. Ser. Map* I-2289 (1992).
52. P. Helfenstein, thesis, Brown University, Providence, RI (1990); *Lunar Planet. Sci.* **XVII**, 333 (1990); P. Schenk and W. McKinnon, *Icarus* **89**, 318 (1989); S. J. Murchie *et al.*, *Lunar Planet. Sci.* **XXIII**, 943 (1992).
53. We thank the current project manager, W. J. O'Neil, and his predecessors J. R. Casani and R. J. Spehalski for their leadership; T. Brady and J. Marr for flight software development and its implementation; G. Levanas and his team for their diagnosis of the tape recorder problems and the creation of a safe way to operate this device; and W. Cunningham and his team who provided the new SSI camera flight software. T. Becker, E. Lee, R. Sucharski, and T. Rosanova provided the team with maps. Many associates of team members contributed to the success of the SSI experiment; we thank N. Ausman, E. A. Alvarez del Castillo, K. Bender, H. Breneman, K. Buxbaum, T. Colvin, D. Deats, T. Denk, S. Fagents, A. DiCicco, P. Helfenstein, S. Henderson, K. Homan, T. Jones, J. M. Kaufman, R. Kirk, J. Klemaszewski, S. LaVoie, E. Lo, L. Lowes, K. Magee, W. Merline, R. Mitchell, H. Mortensen, B. Paczkowski, C. Phillips, K. Rages, A. Simon, D. Simonelli, J. N. Spitale, C. Stanley, E. Ustinov, D. Winther, D. Johnson, J. Van der Woude, J. Yatteau, A. Culver, D. Jensen, D. Alexander, and J. Yoshimizu. We acknowledge the contributions of absent colleagues H. Masursky, J. Pollack, C. Yeates, and J. Dunne. A portion of this research was carried out by the Jet Propulsion Laboratory, California Institute of Technology, under contract with NASA. The National Optical Astronomy Observatories are operated by the Association of Universities for Research in Astronomy (AURA), under cooperative agreement with the National Science Foundation.

24 September 1996; accepted 1 October 1996

Near-Infrared Spectroscopy and Spectral Mapping of Jupiter and the Galilean Satellites: Results from Galileo's Initial Orbit

R. Carlson,* W. Smythe, K. Baines, E. Barbinis, K. Becker, R. Burns, S. Calcutt, W. Calvin, R. Clark, G. Danielson, A. Davies, P. Drossart, T. Encrenaz, F. Fanale,† J. Granahan,† G. Hansen, P. Herrera, C. Hibbitts, J. Hui, P. Irwin, T. Johnson, L. Kamp, H. Kieffer, F. Leader, E. Lellouch, R. Lopes-Gautier, D. Matson, T. McCord,† R. Mehlman, A. Ocampo, G. Orton, M. Roos-Serote, M. Segura, J. Shirley, L. Soderblom, A. Stevenson, F. Taylor, J. Torson, A. Weir, P. Weissman

The Near Infrared Mapping Spectrometer performed spectral studies of Jupiter and the Galilean satellites during the June 1996 perijove pass of the Galileo spacecraft. Spectra for a 5-micrometer hot spot on Jupiter are consistent with the absence of a significant water cloud above 8 bars and with a depletion of water compared to that predicted for solar composition, corroborating results from the Galileo probe. Great Red Spot (GRS) spectral images show that parts of this feature extend upward to 240 millibars, although considerable altitude-dependent structure is found within it. A ring of dense clouds surrounds the GRS and is lower than it by 3 to 7 kilometers. Spectra of Callisto and Ganymede reveal a feature at 4.25 micrometers, attributed to the presence of hydrated minerals or possibly carbon dioxide on their surfaces. Spectra of Europa's high latitudes imply that fine-grained water frost overlies larger grains. Several active volcanic regions were found on Io, with temperatures of 420 to 620 kelvin and projected areas of 5 to 70 square kilometers.

In late June 1996, the Galileo spacecraft obtained its first remote sensing measurements within the jovian system. The Near Infrared Mapping Spectrometer (NIMS) performed spectroscopic and spectral mapping measurements of Jupiter's atmosphere and the surfaces of the Galilean satellites. The NIMS instrument (*1*) has a modest spectral resolving power of 40 to 200 from 0.7 to 5.2 μm, but combines this with spatial coverage at a resolution of 300 to 800 km for Jupiter and a few to several hundred kilometers for the Galilean satellites. A large number of atmospheric molecules, surface minerals, and condensates exhibit diagnostic spectral signatures in the NIMS range, so the measurements represent a powerful tool for investigating